

# An implantable epiretinal device for near-infrared light perception

Received: 19 September 2024

Accepted: 9 March 2026

Published online: 13 April 2026

 Check for updates

Won Gi Chung<sup>1,2,3,10</sup>, Inhea Jeong<sup>1,2,3,10</sup>, Eun-Joo Lee<sup>4</sup>, Gang Cui<sup>5</sup>, Han Jeong<sup>6,7</sup>, Min Seok Choi<sup>6,7</sup>, Sanghoon Lee<sup>1,2,3</sup>, Seung Hyun An<sup>1,2,3</sup>, Eunmin Kim<sup>1,2,3</sup>, Sumin Kim<sup>1,2,3</sup>, Junwon Lee<sup>8</sup>, Suk Ho Byeon<sup>6,7</sup>✉, Sun-Kyung Kim<sup>4</sup>✉ & Jang-Ung Park<sup>1,2,3,9</sup>✉

Human vision relies on photoreceptor cells in the outer retina that are sensitive to visible light. However, many people suffer from blindness due to retinal diseases that cause photoreceptor degeneration. Electrical stimulation of retinal neurons can recreate the action potentials associated with seeing that are generated by these cells. Here we report a thin artificial retina that can be adhered to the epiretinal surface and can convert near-infrared (NIR) light into electrical stimuli that selectively stimulate ganglion cells. The artificial retina consists of a NIR-sensitive phototransistor array and three-dimensional liquid metal micropillar electrodes. The liquid metal electrodes enhance proximity to retinal ganglion cells, providing effective charge injection while minimizing tissue damage, owing to their low Young's modulus. Ex vivo studies demonstrate its biocompatibility, and in vivo studies using healthy and blind mice demonstrate perception of both visible and NIR light, as indicated by cortical recordings and behavioural tests. The retina could, in the future, be used to create a NIR visual channel in patients with photoreceptor degenerative blindness without interfering with their remaining natural vision.

In the mammalian visual system, light within the 400-nm to 700-nm range (visible light) passes through the eye and is detected by sensory neurons, known as photoreceptor cells, in the outer retina<sup>1</sup>. These cells contain light-absorbing pigments, consisting of opsins and their covalently linked retinals. However, detecting longer wavelength light, such as near-infrared (NIR), is much more challenging due to their lower photon energy, which requires opsins with much lower energy barriers. This results in high thermal noise, making NIR visual pigments impractical, and thus there are no instances of mammalian photoreceptors that detect light beyond 700 nm.

Electrical stimulation of inner retinal neurons, such as retinal ganglion cells (RGCs) and bipolar cells, can produce artificial visual percepts. These activations elicit electrical spikes (that is, action potentials) within the retina, identical to when visual information in visible light is transmitted to the brain. Over the past decade, efforts have focused on generating artificial visual perception in people with degenerate photoreceptor cells due to retinal diseases, using photoreactive electronics—electronic retinal prostheses—to restore vision<sup>2–4</sup>.

The integration of optoelectronics with biological systems has developed devices that can interface intimately with mammals,

<sup>1</sup>Department of Materials Science & Engineering, Yonsei University, Seoul, Republic of Korea. <sup>2</sup>Center for Nanomedicine, Institute for Basic Science (IBS), Seoul, Republic of Korea. <sup>3</sup>Graduate Program of Nano Biomedical Engineering (NanoBME), Advanced Science Institute, Yonsei University, Seoul, Republic of Korea. <sup>4</sup>Department of Applied Physics, Kyung Hee University, Gyeonggi-do, Republic of Korea. <sup>5</sup>Ophthalmology Division, Jiangsu Kerbio Medical Technology Group Co. Ltd., Changzhou, China. <sup>6</sup>Institute of Vision Research, Department of Ophthalmology, Severance Eye Hospital, College of Medicine, Yonsei University, Seoul, Republic of Korea. <sup>7</sup>Brain Korea 21 Project for Medical Sciences, College of Medicine, Yonsei University, Seoul, Republic of Korea. <sup>8</sup>Institute of Vision Research, Department of Ophthalmology, Gangnam Severance Hospital, Yonsei University College of Medicine, Seoul, Republic of Korea. <sup>9</sup>Department of Neurosurgery, College of Medicine, Yonsei University, Seoul, Republic of Korea. <sup>10</sup>These authors contributed equally: Won Gi Chung, Inhea Jeong. ✉ e-mail: [shbyeon@yuhs.ac.kr](mailto:shbyeon@yuhs.ac.kr); [sunkim@khu.ac.kr](mailto:sunkim@khu.ac.kr); [jang-ung@yonsei.ac.kr](mailto:jang-ung@yonsei.ac.kr)

including humans<sup>5–7</sup>. As therapeutic technologies improve, these could lead to both restored and healthy abilities<sup>8</sup>, facilitating the restoration of deficient abilities or creating new ones, such as detection of NIR light. Enabling detection of NIR light could provide a way of supplementing light sensitivity in affected retinal regions without interfering with the visible vision that remains. For example, a clinical study has shown that patients with age-related macular degeneration were able to simultaneously use prosthetic central vision and natural peripheral vision, demonstrating that artificial and natural visual modalities can coexist<sup>8</sup>. It could also have potential applications, such as enhancing daylight vision, improving early disease detection through medical imaging and providing precise neural modulation by optogenetic therapies.

In this article, we report a flexible implantable artificial retina for perception in the NIR range. It consists of an array of thin photosensitive transistors covered by a NIR-transmission filter and soft three-dimensional (3D) stimulation electrodes made of liquid metal (LM). The thin (360 nm) transmission filter selectively detects NIR light while blocking visible light. The photosensitive transistors then convert the NIR light into electrical stimuli and deliver it to the retinal neurons of the eye through pillar-shaped 3D LM electrodes. These low-modulus, biocompatible electrodes conform to the non-uniform retinal surface, enhancing proximity to target RGCs and reducing stimulation thresholds. In addition, platinum nanoclusters on the electrode tips provide reduced impedance and effective charge injection. Selective stimulation can be achieved through varying the pillar heights of the electrodes.

Our device is designed for epiretinal implantation (Supplementary Fig. 1), offering easier surgical access compared with subretinal approaches<sup>3,9</sup>. Biocompatibility studies using human retinal pigment epithelium (RPE) cells show negligible side effects. Furthermore, we demonstrate implantation of our artificial retina onto the inner retinal surfaces of healthy and retinal degenerative mice. Simultaneous electrophysiological recordings from the mice retina and visual cortex show that signal amplification during NIR-light illumination led to an increase in real-time neural responses. This confirms that both the retina and visual cortex of healthy and blind mice with the artificial retina are activated by NIR light. Our device could thus extend mammalian vision into the NIR, opening up possibilities for expanded human sensory capabilities, and offering practical applications such as perceiving thermal signatures.

## NIR-perceptive artificial retina

Figure 1a illustrates the anatomical structure of the retinal tissues where our NIR-perceptive artificial retina device is implanted close to the retinal surface. The device integrates an array of photosensitive transistors covered by a thin patterned NIR-transmission filter (thickness: 360 nm) and soft 3D microelectrodes (height: 60  $\mu\text{m}$ , diameter: 20  $\mu\text{m}$ ) made of LMs. The artificial retina conformably attaches to the innermost surface of the retina, with the 3D LM electrodes directly stimulating RGCs. When NIR light passes through the filter, it generates photocurrents within the semiconductor channel, leading to amplification of the drain current ( $I_D$ ). This amplified  $I_D$  greatly increases the charge injection to RGCs through the 3D microelectrodes with pulsed stimuli of drain voltage ( $V_D$ ). The protruding pillar shape of the electrodes focuses electric fields on their tips, inducing neural responses more efficiently, compared with stimulation electrodes with a flat surface-type structure (Supplementary Fig. 2)<sup>10</sup>. To expand the mammalian visual spectrum into the NIR range while preserving original visible-light vision, we photolithographically patterned the NIR-transmission filter to allow visible light to pass through specific areas of our device while blocking it from the photosensitive channels of the phototransistors (Supplementary Fig. 3). This design enables the semiconductor channels to generate photocurrents only in response to NIR-light intensity, while allowing visible light to activate photoreceptor cells in the filter-free areas. As illustrated in Fig. 1b,

visible light transmits through the gaps between the filter patterns (spacing: 40  $\mu\text{m}$ ), optically stimulating visible-light-perceptive photoreceptor cells. Conversely, NIR light activates the NIR-responsive phototransistors, generating photocurrents that electrically stimulate RGCs by means of the 3D LM electrodes connected to the drain pads. Consequently, the action potentials evoked within the RGCs can be transmitted to the visual cortex through the optic nerve, expanding the visual spectrum into the NIR range. Figure 1c illustrates a schematic layout of the NIR-perceptive artificial retina device. The phototransistors consist of single-crystalline Si channels (thickness: 1,500 nm), Cr/Au/Pt source/drain electrodes (thickness: 5/100/30 nm), a transparent SiO<sub>2</sub> dielectric layer (thickness: 1,300 nm) and transparent indium tin oxide (ITO) gate electrodes (thickness: 150 nm). Figure 1d shows a scanning electron microscope (SEM) image of the amorphous Si (a-Si)/SiO<sub>2</sub> NIR-transmission filter pattern positioned on the opposite side of the phototransistors. The 3D protruding micropillars of LM (EGaIn) were directly printed on the open surface of the drain pads using a capillary nozzle to form the stimulation electrodes. After coating a parylene C layer (thickness: 1  $\mu\text{m}$ ) on the entire sidewall of the 3D LM pillars, their tips were locally opened using an anisotropic reactive ion etching (RIE) process to selectively deposit Pt nanoclusters on the tips. The detailed fabrication processes of the NIR-perceptive artificial retina are described in Supplementary Fig. 4 and Methods. The detailed design, optical properties and fabrication processes of the NIR-transmission filter are described in Methods and the Supplementary Information. A photo of the device is shown in Fig. 1e.

Cell viability and apoptosis tests were conducted to investigate the biocompatibility of the artificial retina. For the cytotoxicity test, the apoptosis assay was conducted using flow cytometry (Fig. 1f). We measured the cell viability by seeding human RPE cells on the fabricated sample. For comparison, human RPE cells were also seeded on the references, negative control (a 1- $\mu\text{m}$ -thick parylene C film with no 3D microelectrodes), positive control (cells with puromycin) and samples with the 3D microelectrodes. Human RPE cells grown on these electrode samples showed high viability (99.4%, Fig. 1g). The viability of cells grown on the parylene C film as a negative control was 98.5%, whereas puromycin-treated cells as a positive control showed a much lower viability of 4.01%. These results indicate that our artificial retina did not exhibit notable cytotoxicity, satisfying the *in vitro* cytotoxicity standard (>80%) for medical devices (ISO 10993-5)<sup>11</sup>.

To evaluate the long-term *in vivo* safety and stability of the device with 3D LM microelectrodes, immunohistochemical assays and cryosection imaging were conducted on eyeballs extracted from wild-type (WT) mice ( $n = 3$ ) six months after implantation of the NIR-perceptive artificial retina (without interconnections). As shown in Supplementary Fig. 5, the device remained stably positioned on the retinal surface without tilting or collapsing, and the 3D LM microelectrode tips were properly positioned within the RGC layer, with no signs of malignancy or inflammation. The immunohistochemical analysis also revealed preserved fluorescence signals for RGC markers and no notable gliosis or microglial activation (Supplementary Fig. 6), supporting the long-term biocompatibility of the artificial retina. Additional methodological details are provided in the Supplementary Information.

## Optoelectrical and electrochemical characteristics of the artificial retina

Supplementary Figs. 7a,b illustrate the transfer and output characteristics, respectively, of our silicon field-effect transistor (FET) without light exposure. The mobility was calculated as  $-166 \text{ cm}^2 \text{ V}^{-1} \text{ s}^{-1}$ , the on/off ratio ( $I_{\text{on}}/I_{\text{off}}$ ) as  $4.41 \times 10^6$  and the threshold voltage ( $V_{\text{th}}$ ) as 4.08 V. The statistical analysis of the field-effect mobility,  $I_{\text{on}}/I_{\text{off}}$ , and  $V_{\text{th}}$  of a  $50 \times 50$  Si phototransistor array (2,500 pixels) is provided in Supplementary Fig. 8, and these data follow Gaussian profiles. The calculations of these characteristics are described in the Supplementary Information. As plotted in Fig. 2a,b, the transfer ( $V_D = 5 \text{ V}$ ) and output

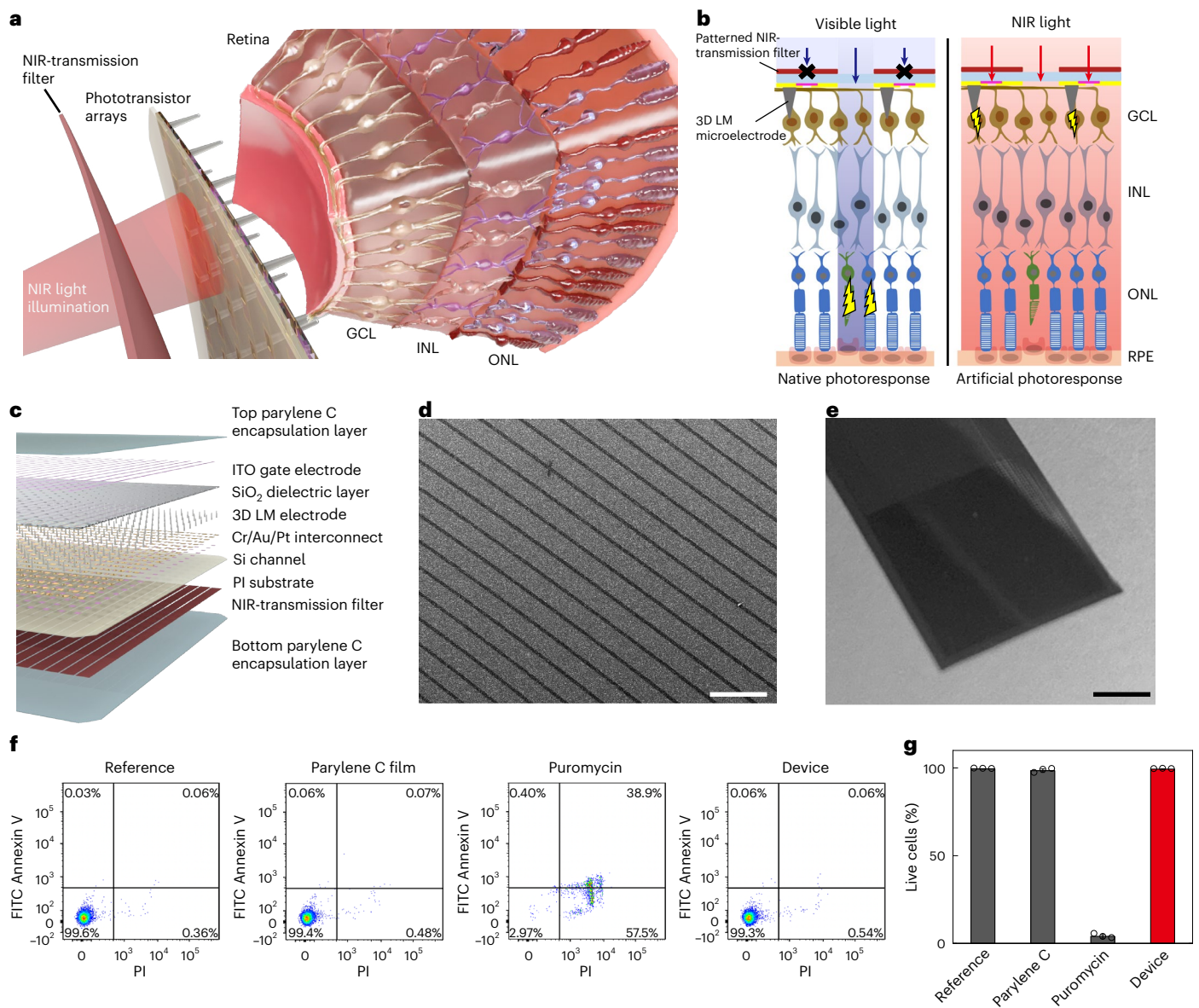


**Fig. 1 | NIR-perceptive artificial retina. a**, Schematic of the NIR-perceptive artificial retina with the NIR-transmission filter and phototransistor arrays. **b**, Detailed schematic of the artificial retina with the NIR-transmission filter and phototransistor arrays, illustrating how NIR light is detected and converted into electrical signals to stimulate retinal neurons. **c**, Schematic of the layouts of the artificial retina based on the integration of photosensitive transistors with 3D LM electrodes. **d**, SEM image of the NIR-transmission filter. The grey part blocks visible light and the black part transmits visible light. Scale bar, 100 μm.

The experiment was repeated ten times with similar results. **e**, Photograph of the fabricated NIR-sensitive phototransistor array integrated with the NIR-transmission filter. Scale bar, 1 mm. The experiment was repeated ten times with similar results. **f**, Flow cytometry analysis for cell viability. **g**, Quantitative analysis of live cells (%) for each condition from **f**. Data presented as mean  $\pm$  s.d.  $n = 3$  biological replicates, each representing an independent sample. GCL, ganglion cell layer; INL, inner nuclear layer; ONL, outer nuclear layer; PI, propidium iodide.

characteristics ( $V_G = 70$  V) show typical light-sensitive FET behaviour when illuminated with NIR light (wavelength: 900 nm) of intensities ranging from 0 to 1.2 mW cm<sup>-2</sup>. The range of the NIR-light intensities was set as environmental indoor NIR-light levels<sup>12</sup>. The inset of Fig. 2b shows the output characteristics in the cutoff range ( $V_G = -20$  V). As the level of the drain current ( $I_D$ ) and the sensitivity of the FETs were optimal for retina stimulation (1–20 μA), we selected this range for the operation of the artificial retina to ensure appropriate stimulation parameters for the retina. Figure 2c shows the real-time detection of incident light ( $V_D = 5$  V,  $V_G = -20$  V and light intensity of 1.0 mW cm<sup>-2</sup>), and both the response and recovery time of the phototransistor was 10 ms. As shown in Fig. 2d, the relative changes in  $I_D$  of the Si phototransistor arrays ( $\Delta I_D/I_D$ ) exhibit a linear relationship with

the intensity of incident light ( $I_0$  is  $I_D$  at the dark state and  $\Delta I_D = I_D - I_0$ ). This suggests that our device can stimulate the retina based on the intensity of the incident light. Furthermore, Fig. 2e shows the relative change in  $I_D$  of the Si phototransistor arrays as a function of light wavelength ranging from 350 nm to 1,000 nm with the NIR-transmission filter.

Low-modulus materials are essential for biomedical implants to minimize tissue damage and improve biocompatibility. LMs, with Young's modulus below 300 kPa (compared with GPa for rigid solid-phase metals), offer a major advantage as bioelectrodes<sup>13–17</sup>. This low modulus allows LM electrodes to conform to a soft tissue environment, reducing mechanical mismatch and subsequent stress-induced inflammation or scarring, while maintaining excellent electrical neural

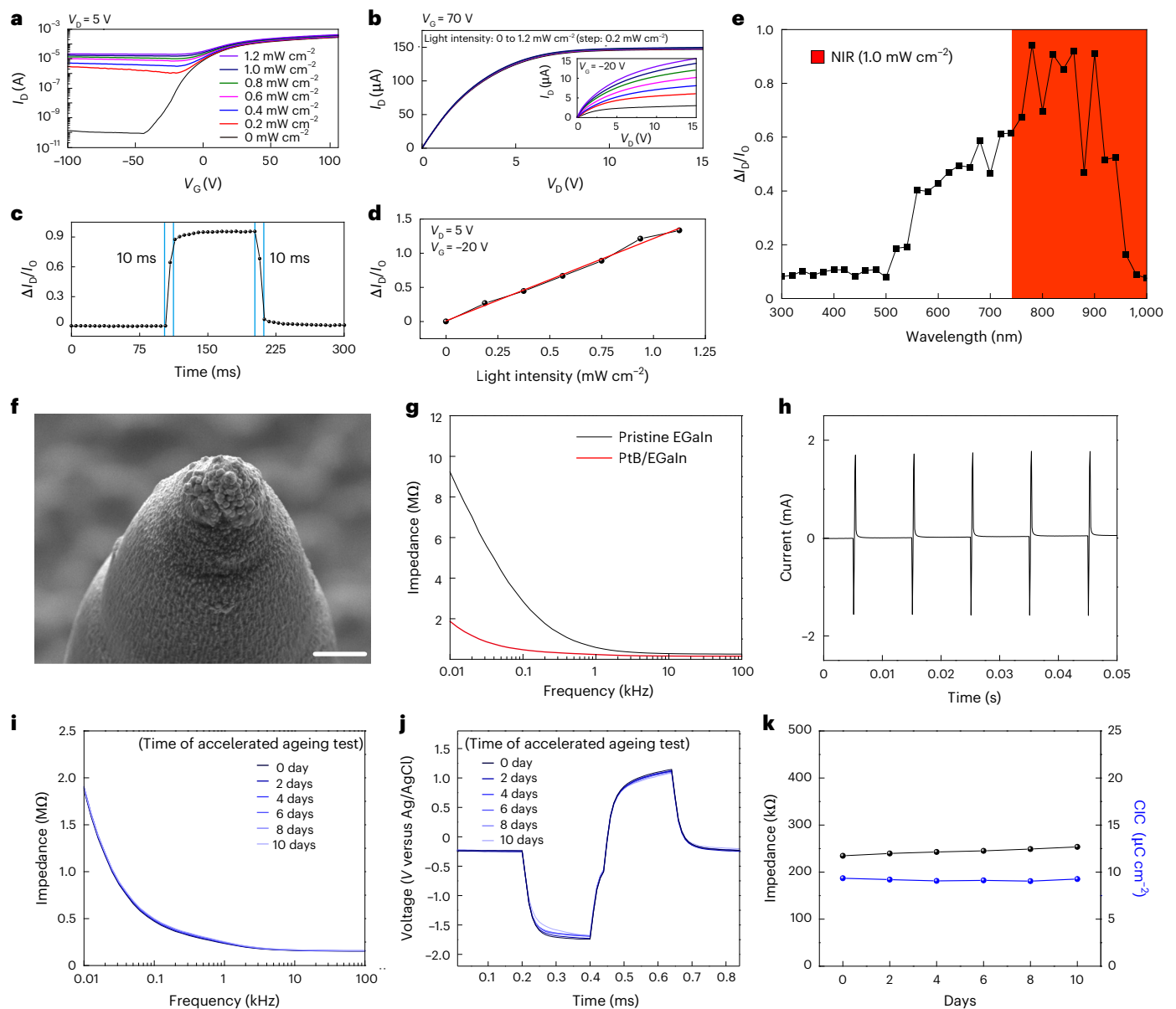


**Fig. 2** Optoelectronic and electrochemical properties. **a**, Transfer characteristics under stepwise irradiation of NIR light (intensities of 0, 0.2, 0.4, 0.6, 0.8, 1.0, 1.2  $\text{mW cm}^{-2}$  at 900 nm) at  $V_D$  of 5 V. **b**, Output characteristics under stepwise irradiation of NIR light (intensities of 0, 0.2, 0.4, 0.6, 0.8, 1.0, 1.2  $\text{mW cm}^{-2}$  at 900 nm) at saturation region ( $V_G = 70$  V). The inset shows the output characteristics in the cutoff region ( $V_G = -20$  V). **c**, Response time of the phototransistor arrays at  $V_D = 5$  V,  $V_G = -20$  V under light irradiation (intensity of 1.0  $\text{mW cm}^{-2}$  at 900 nm). **d**, Relative changes in  $I_D$  of the phototransistor array as a function of light intensities at  $V_D = 5$  V,  $V_G = -20$  V. The slope of the plot represents the responsivity of the device. **e**, Relative changes in  $I_D$  of the phototransistor array as a function of light wavelength with NIR-transmission filter at  $V_D = 5$  V,

$V_G = -20$  V. **f**, SEM image of Pt nanoclusters locally coated on the tip of the 3D LM electrode. Scale bar, 1  $\mu\text{m}$ . The experiment was repeated twenty times with similar results. **g**, Impedance spectroscopy of 3D LM electrodes. **h**, Typical stimulation pulses using our 3D LM electrodes. **i**, Impedance spectroscopy of 3D LM electrodes at 1-day intervals over 10 days under accelerated ageing test environments. **j**, Voltage transients in response to biphasic pulses (pulse width, 200  $\mu\text{s}$ ; interphase delay, 40  $\mu\text{s}$ ; current amplitude, 15  $\mu\text{A}$ ) measured daily under accelerated ageing test environments over 10 days. **k**, Changes in impedance at 1-kHz frequency and CIC values over 10 days under accelerated ageing environments.

interfaces. The modulus of our 3D LM electrodes (236 kPa with parylene C sidewalls and Pt nanocluster tips) was comparable with that of the tissues in the eye, such as the sclera, cornea and retina<sup>18–20</sup>. By contrast, as shown in Supplementary Fig. 9, the modulus of rigid solid-type materials used as conventional stimulation electrodes, is at least three orders of magnitude higher than that of biological tissues, potentially causing retinal damage. In this work, 3D micropillar-shaped EGaIn electrodes were directly printed for recording and stimulation purposes (see Methods for the details of the printing procedures). Figure 2f shows an SEM image of the Pt nanoclusters locally coated only on the tip of

our 3D LM electrodes. To use these electrodes for retinal stimulation, their electrochemical properties were measured by electrochemical impedance spectroscopy and cyclic voltammetry (CV) analysis using a multichannel potentiostat (Parstat MC-1000, AMETEK, USA). All electrodes were immersed in a phosphate-buffered saline (PBS) solution (pH 7.4) under ambient conditions, with an Ag/AgCl electrode and a Pt sheet used as reference and counter electrodes, respectively. Figure 2g plots the impedance of the 3D LM electrodes (height: 60  $\mu\text{m}$ ) by sweeping the frequencies from 10 Hz to 100 kHz, presenting an impedance of 210 k $\Omega$  (at 1 kHz) for an electrode area of 32.1  $\mu\text{m}^2$ . This impedance

was approximately three times lower than that of the Pt-uncoated sample. Supplementary Fig. 10 shows the CV characteristics of the 3D electrodes with Pt nanoclusters measured at a scan rate of  $50 \text{ mV s}^{-1}$  with a potential limit range from  $-0.6 \text{ V}$  to  $0.8 \text{ V}$ . The negative area enclosed by the CV curves presents their cathodic charge storage capacity ( $34.28 \text{ mC cm}^{-2}$  for the electrode area of  $32.1 \mu\text{m}^2$ ). As shown in Fig. 2h, a typical stimulating pulse signal (pulse width =  $1 \text{ ms}$ , frequency =  $10 \text{ Hz}$ ,  $V_D = 1 \text{ V}$ ) was recorded by a recording electrode placed adjacent to the stimulation electrode (distance between electrodes:  $40 \mu\text{m}$ ) when a voltage-controlled monophasic cathodic pulse was applied to the stimulation electrode. The charge injection capacity (CIC) was calculated as  $9.35 \text{ mC cm}^{-2}$ . Electrochemical impedance spectroscopy was then conducted at one-day intervals to monitor impedance changes at  $1 \text{ kHz}$  (Fig. 2i). Over a ten-day period, corresponding to approximately ten months under physiological conditions, the impedance at  $1 \text{ kHz}$  showed only a slight increase, from  $234.6 \text{ k}\Omega$  to  $253.59 \text{ k}\Omega$ . In addition, under accelerated ageing conditions, the CIC remained stable, decreasing only marginally from  $9.35 \text{ mC cm}^{-2}$  to  $9.04 \text{ mC cm}^{-2}$  over the same period (Fig. 2j), demonstrating the good long-term electrical stability of the device (Fig. 2k).

### Ex vivo evaluation of retinal responses

We conducted an ex vivo evaluation of retinal responses by stimulation and in situ neural recording of RGC responses in mice retinas under NIR-light illumination using our artificial retina device (consisting of the NIR-transmission filter, phototransistors and LM electrodes). For this ex vivo recording, isolated small pieces of retinas ( $4 \times 4 \text{ mm}$ ) from both WT (C57BL/6J, Japan SLC,  $n = 5$ ) and retinal degenerative (rd1) (C3H/C3H/HeNcrOri, Japan SLC,  $n = 5$ ) mice were directly placed on our device (consisting of 36 stimulating and recording electrode pairs), with 3D LM electrodes directed towards the RGC side of the retina in PBS media. The 3D LM electrode height was optimized to  $60 \mu\text{m}$ , based on the distance from the epiretinal surface to the RGCs in mice retina (Supplementary Table 1), to ensure that the electrode tips directly interfaced with the target cells (Supplementary Fig. 5) and to achieve maximum RGC firing activity during electrical stimulation, as determined by our previous study<sup>21</sup>. Figure 3a presents a schematic illustration of this experimental set-up, and Fig. 3b illustrates the interface of our device with retinal layers. The position of the retina (with light exposure from the retina side) allowed native retinal responses from photoreceptor cells of the WT retina to visible light, despite the presence of the NIR-transmission filter and the FET gate, a  $2\text{-}\mu\text{m}$ -thick insulating layer of SU-8 was sandwiched between these two components. As plotted in Supplementary Fig. 11, the insertion of the SU-8 layer did not reduce the NIR absorption of the Si channel in the FET<sup>22</sup>. For recording retinal responses (that is, optically evoked or electrically evoked retinal spike potentials and firing rate of the spikes), each recording electrode was positioned adjacent to each stimulating electrode (pitch between the stimulating and recording electrodes:  $40 \mu\text{m}$ ). For electrically stimulating the retina, the FETs were operated with a specific condition ( $V_D$ : pulsed bias of  $3 \text{ V}$  with a pulse duration of  $1 \text{ ms}$  and frequency of  $10 \text{ Hz}$ ,  $V_G$ : d.c. bias of  $-20 \text{ V}$ ). Detailed experimental procedures and set-up for ex vivo experiments are provided in the Methods. As plotted in Fig. 3c, the neural activity of RGCs, such as optically evoked potentials (OEPs) and firing rates of RGC spikes, in WT mice retina were recorded under exposure to visible light (wavelength:  $470 \text{ nm}$ , intensity:  $1.2 \text{ mW cm}^{-2}$ ) and NIR light (wavelength:  $900 \text{ nm}$ , intensity:  $1.2 \text{ mW cm}^{-2}$ ) without operating FETs. Although WT mice retinas negligibly responded to NIR light, they exhibited robust firing of RGCs in the visible light. Using WT mice retinas, we recorded their OEPs without the FET operation under the illumination of visible light or NIR light. For comparison, the retinas' electrically evoked potentials (EEPs) stimulated by operating our FETs ( $V_D$ : pulsed bias of  $3 \text{ V}$  with a pulse duration of  $1 \text{ ms}$  and frequency of  $10 \text{ Hz}$ ,  $V_G$ : d.c. bias of  $-20 \text{ V}$ ) were

also recorded for identical illumination conditions. These OEP and EEP signals were obtained at a  $25\text{-kHz}$  sampling rate using a  $300\text{-Hz}$  low-pass and a  $3\text{-kHz}$  high-pass filter. As shown in Fig. 3d, the OEP magnitude of the WT retina under NIR illumination was negligible, in contrast with the OEP magnitude of  $92 \mu\text{V}$  for the visible-light-exposure case, indicating that NIR-light illumination did not induce retinal responses within the WT retina.

When the FETs in the retina were operating, however, both visible-light and NIR-light exposure showed distinctive EEP signals with similar magnitudes ( $88 \mu\text{V}$  and  $86 \mu\text{V}$ , respectively). Figure 3d demonstrates that the operation of our device generated similar levels of EEP signals from the WT retina when irradiating both visible light (natural ability) and NIR light (artificial ability). Figure 3e,f shows the neural activities (that is EEPs (top insets) and firing rates (bottom)) of both WT and rd1 mice retinas, respectively, with operating FETs under NIR-light exposure of different intensities ranging from  $0$  to  $1.2 \text{ mW cm}^{-2}$ . As shown in Fig. 3g, firing rates of RGC spikes increased with light intensity in both WT and rd1 retinas. Furthermore, these EEP signals demonstrated that the electrical stimulation provided by our device induced neural responses in both WT and rd1 retinas at levels comparable to the natural OEP signals generated during visible-light exposure without FET operation. This indicates that our device effectively translates NIR-light input into neural responses similar to those naturally produced by visible light in healthy retinas. In addition, the firing rates showed negligible differences between the WT retina and the rd1 retina. This similarity can be attributed to the fact that the WT retina does not exhibit intrinsic photoreponses to NIR light in its functional photoreceptor layers. Consequently, both WT and rd1 retinas rely on the artificial stimulation provided by our device to respond to NIR light, resulting in comparable neural activities.

### In vivo induction of NIR vision in retinal degenerative and WT mice

To validate that our artificial retina device can induce NIR visual perception in living mice, we conducted in vivo experiments using both rd1 mice (blind,  $n = 3$ ) and WT mice (normal vision,  $n = 3$ ), after implanting our artificial retina onto their epiretinal surfaces. In addition, deep brain probes were implanted into the brains of these mice, specifically targeting the primary visual cortex for cortical recording and the frontal lobe for reference (Fig. 4a). When the retina perceives light, the optical signal transitions to an electrical form, passes through the optic nerve and the lateral geniculate nucleus, and reaches the visual cortex. We implanted commercial tungsten brain probes to target layer four of the visual cortex, where the electrical signal is first processed. This layer was chosen as the recording site owing to its known robust signal compared with other layers within the visual cortex<sup>20</sup>. Detailed implantation procedures for the brain probes are described in the Methods. Considering the eyeball size of the mouse ( $\sim 3 \text{ mm}$  in diameter), we fabricated an artificial retina device with a  $6 \times 6$  array of Si phototransistors (pixel pitch:  $500 \mu\text{m}$ , device dimension:  $1 \text{ mm}$  in width), integrated with the NIR-transmission filter and 3D LM electrodes. This device was then implanted onto the mouse's retinal surface with external interconnections. Figure 4b shows a photograph of a WT mouse after implantation of both brain probes and our artificial retina device. Our device adhered well to the retinal surface of the mouse without causing notable damage or bleeding. A cross-sectional optical coherence tomography (OCT) image obtained post surgery reveals the anatomical morphology of the retinal surface near our 3D LM electrodes (Fig. 4c). To obtain a clear cross-sectional OCT image, only the 3D microelectrodes (height:  $60 \mu\text{m}$ , diameter:  $20 \mu\text{m}$ ) formed on an  $8\text{-}\mu\text{m}$ -thick PI film were implanted onto the retinal surface, preventing image distortion due to reflections from other device components (for example, NIR-transmission filter, FETs and other interconnect metals). This OCT image confirmed that our 3D microelectrodes were conformally surrounded by retinal tissues (with the interface between

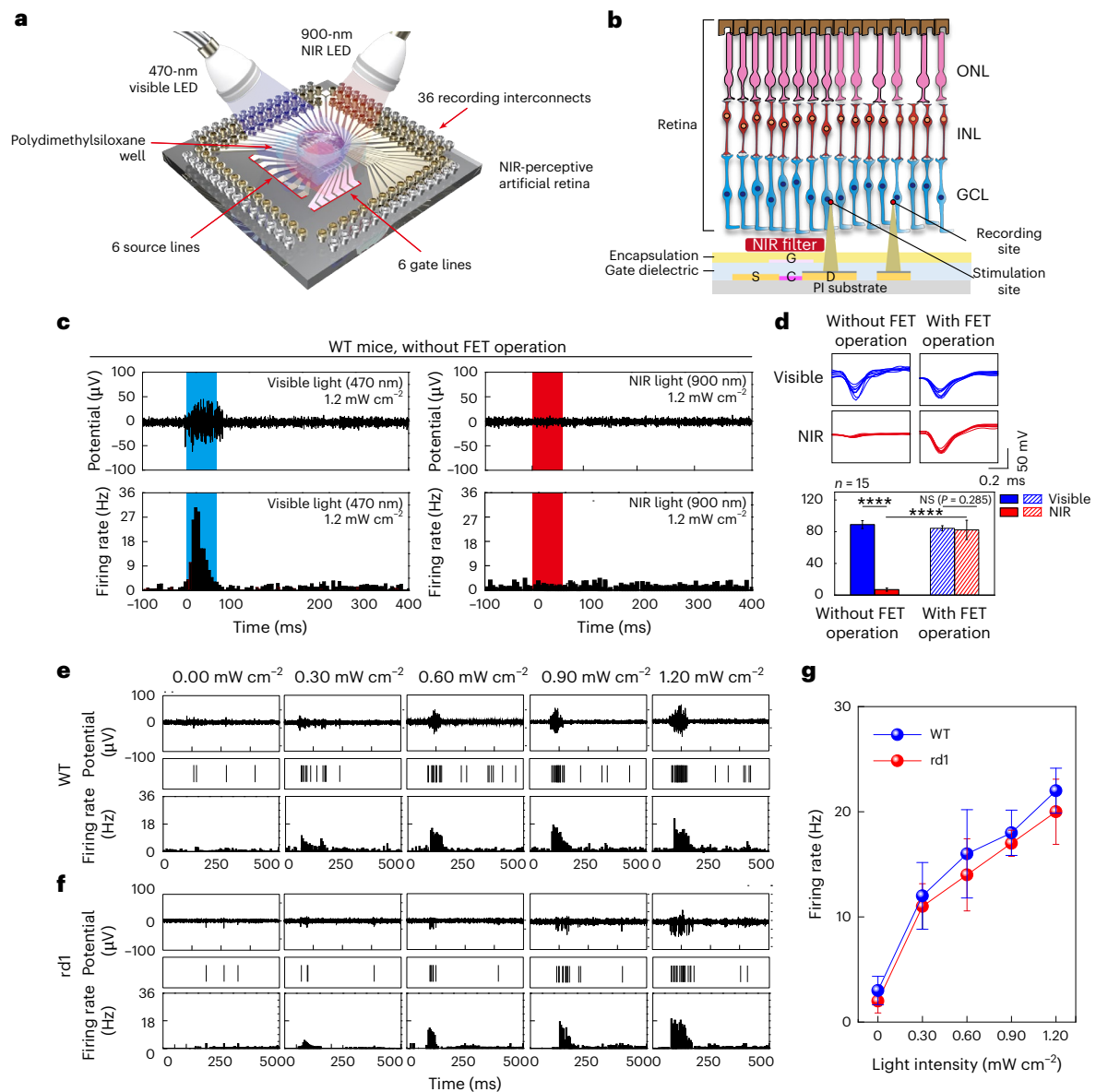


**Fig. 3 | Ex vivo evaluation of retinal responses.** **a**, Schematic illustration of experimental set-up for an ex vivo experiment using WT and rd1 mouse retinas. **b**, Schematic illustration of experimental set-up for an ex vivo experiment using WT mouse retinas. **c**, Neural responses of evoked RGC spikes of WT mouse retina under visible light and NIR light without device operation. **d**, Comparison of the electrical potentials between NIR light and visible light during device operation with and without device operation from WT mouse retina. Data are presented as mean  $\pm$  s.d.;  $n = 15$  independent experiments. Statistical significance was evaluated using an unpaired one-tailed Student's  $t$ -test; not significant (NS); \*\*\*\* indicates  $P < 0.0001$ ; exact  $P$  values are provided in the source data.

**e**, Neural responses of evoked RGC spikes of WT mouse retina under the various intensities of light illumination (wavelength of 900 nm, intensities of 0, 0.3, 0.6, 0.9, 1.2  $\text{mW cm}^{-2}$ ) during the operation of the NIR-perceptive artificial retina with 3D LM electrodes (height, 60  $\mu\text{m}$ ). **f**, Neural responses of evoked RGC spikes of rd1 mouse retina under the various intensities of light illumination (wavelength of 900 nm, intensities of 0, 0.3, 0.6, 0.9, 1.2  $\text{mW cm}^{-2}$ ) during the operation of the NIR-perceptive artificial retina with 3D LM electrodes (height, 60  $\mu\text{m}$ ). **g**, Firing rates of evoked RGC spikes as a function of illuminated light intensities for WT and rd1 mouse retina. Data are mean  $\pm$  s.d. with  $n = 5$  biologically independent mice.

their tips and RGCs) without collapsing. For simultaneous stimulation and recording using our device, each pixel consisted of a phototransistor with a stimulation electrode and a recording electrode, with the recording electrode adjacent to the stimulation electrode at a pitch of 40  $\mu\text{m}$  (Supplementary Fig. 12).

We used two light sources (visible: wavelength of 470 nm, NIR: wavelength of 900 nm, commercial light-emitting diodes (LEDs)) projected sequentially onto the fundus of the mouse eye. Before the experiment, we confirmed the complete degeneration of the photoreceptor layer in 8-week-old rd1 mice through histology analysis (Supplementary Fig. 13). Detailed experimental procedures, including anaesthesia and surgery processes, are provided in the Methods.

For both rd1 mice and WT mice, we exposed NIR light to the fundus of the eye for 1 s, rested for 3 s, and then exposed visible blue light to the fundus of the eye for 1 s. As illustrated in Fig. 4d, for the rd1 mouse, the photoreceptor cells were fully degenerated, indicating that the mouse could perceive visible light. However, due to the activation of RGCs stimulated by our artificial retina device under NIR exposure, the rd1 mouse was able to perceive NIR light, as evidenced by the cortical recordings plotted in Fig. 4e. Figure 4f quantitatively compares the retinal responses (that is, firing rates) elicited after the exposure of NIR and visible light, with or without operating our artificial retina device. As expected, neither NIR nor visible light could elicit retinal responses in the rd1 mouse without operating our device. However,

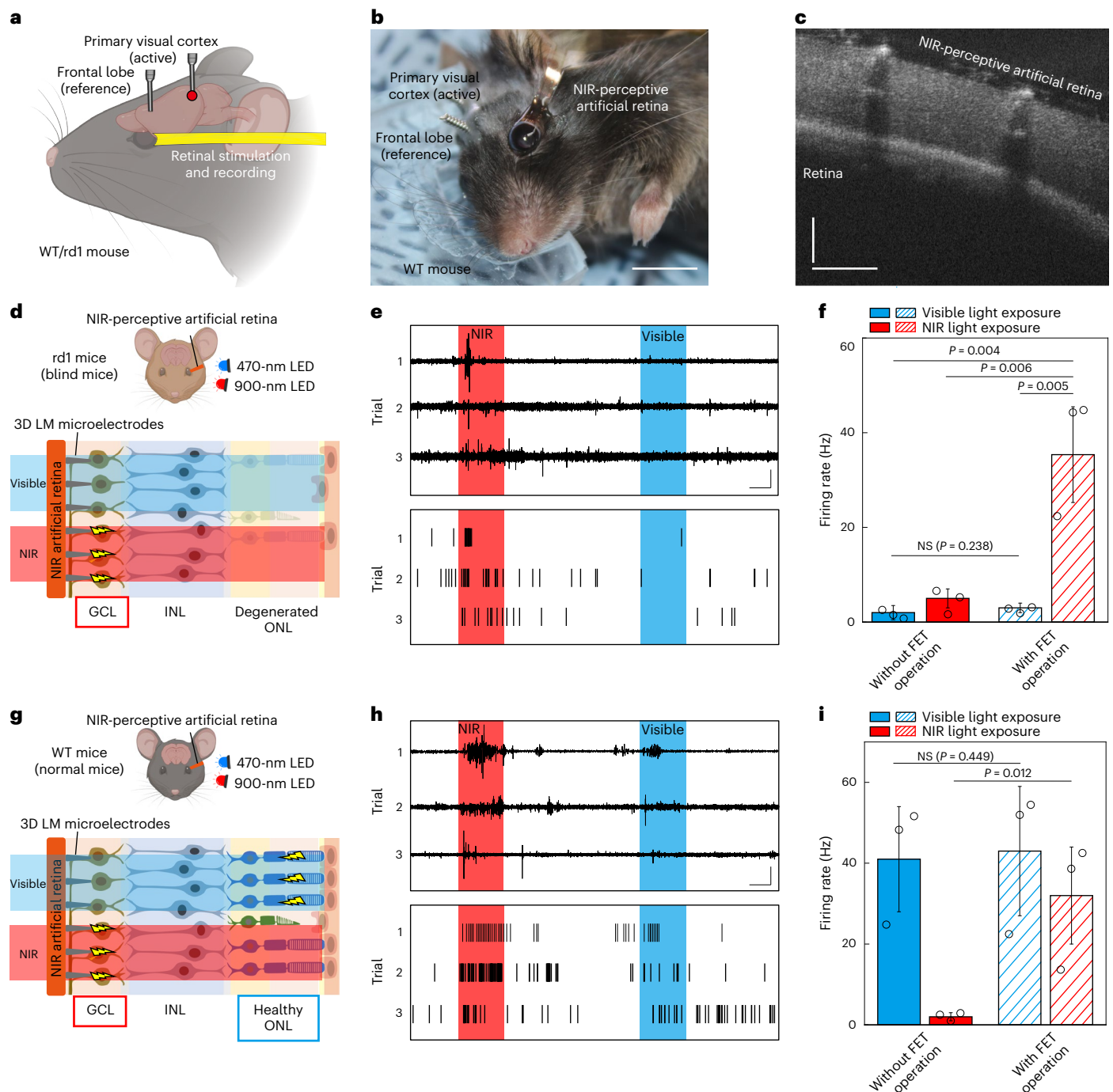


**Fig. 4 | In vivo induction of NIR vision in both rd1 and WT mice.** **a**, Schematic illustration of the experimental set-up of the in vivo experiment using both rd1 mice and WT mice. **b**, Photograph of experimental set-up during the in vivo experiment using the live WT mouse. Scale bar, 6 mm. **c**, OCT image of the WT mouse retina after device implantation. OCT image shows the retinal tissues surrounding the 3DLM electrodes. Scale bar, 100  $\mu\text{m}$ . **d**, Schematic illustrations of in vivo animal experiments using rd1 mice with visible-light illumination (wavelength, 470 nm) and NIR light (wavelength, 900 nm). **e**, Cortical responses from the mouse visual cortex (raw traces of single-unit RGC spikes and corresponding raster plots) during the operation of the artificial retina under constant visible-light illumination (wavelength, 470 nm) and NIR light (wavelength: 900 nm). Scale bars, horizontal, 200 ms; vertical, 100  $\mu\text{V}$ . **f**, Quantitative comparison of the firing rate from the visual cortex in rd1 mice with and without the NIR-device operation under NIR and visible-light

stimulation. Data are presented as mean  $\pm$  s.d.;  $n = 3$  biologically independent mice. Statistical significance was evaluated using an unpaired one-tailed Student's  $t$ -test; NS. **g**, Schematic illustrations of in vivo animal experiments using WT mice with visible-light illumination (wavelength, 470 nm) and NIR light (wavelength, 900 nm). **h**, Cortical responses from the mouse visual cortex (raw traces of single-unit RGC spikes and corresponding raster plots) during the operation of the artificial retina under constant visible and NIR-light illumination. Scale bars, horizontal, 200 ms; vertical, 100  $\mu\text{V}$ . **i**, Quantitative comparison of the firing rate in WT mice with and without the NIR-device operation under NIR and visible stimulation. Data are presented as mean  $\pm$  s.d.;  $n = 3$  biologically independent mice. Statistical significance was evaluated using an unpaired one-tailed Student's  $t$ -test; NS. Mouse illustrations in **a**, **d** and **g** created in BioRender; Chung, W. (2026): <https://biorender.com/lji5rqi> (**a**), <https://biorender.com/uij8lhb> (**d**, **g**).

with device operation, cortical responses from the rd1 mouse showed robust activities only upon NIR-light exposure, indicating that our artificial retina device can selectively stimulate under different types of light (that is, visible light and NIR).

It is important to not only create this new ability (NIR visual perception), but also for it to coexist with the original abilities (visible-light perception). For the WT mouse, the remaining healthy photoreceptor cells could only detect visible light (Fig. 4g). However, due to the effective stimulation of our artificial retina device upon incident NIR light, robust activities from the visual cortex were observed from both visible and NIR light (Fig. 4h). The electrophysiological activation of the retinal neurons induced rapid cortical responses comparable with normal vision (visible-light perception with photoreceptors). Before the device operation, there was a large difference between the retinal responses (that is, firing rates) after visible-light and NIR-light exposure. However, after the device operation, the retinal responses to NIR exposure greatly increased, becoming comparable with that of the visible-light case (Fig. 4i). Supplementary Fig. 14 shows real-time neural responses of RGC spikes (that is, traces of spike potentials and firing rates of evoked spikes) in WT mice under constant NIR-light illumination (intensity of  $1.2 \text{ mW cm}^{-2}$ ). In contrast with negligible neural responses without operating FETs, the FET operation generated RGC spikes in all pixels upon NIR-light exposure, presenting good uniformity in the firing rates recorded from all 36 pixels. For example, Supplementary Fig. 15 plots the statistical analysis of firing rates upon NIR illumination, and these data follow Gaussian profiles. Similar responses with good uniformity were also recorded from all 36 pixels under visible-light illumination. These results demonstrate the perception of both visible and NIR light, effectively broadening the visual spectrum to include naturally invisible NIR light in both normal and blind mice models.

To assess light-guided behaviour using two different visual modalities, we conducted a head-fixed behavioural task in water-restricted WT mice ( $n = 5$ ) and rd1 mice ( $n = 5$ ), either implanted with the NIR-perceptive artificial retina or serving as non-implanted controls. In this task, either NIR or visible-light pulses were presented as visual cues predicting delayed water delivery (Extended Data Fig. 1a). The anticipatory lick rate, defined as lick responses occurring after the light cue but before water delivery, was used as a behavioural readout. As shown in Extended Data Fig. 1b, implanted rd1 mice exhibited strong anticipatory responses specifically to NIR cues, confirming the presence of NIR-based visual behaviour. By contrast, non-implanted control mice did not show anticipatory licking in response to NIR stimuli. Extended Data Fig. 1c,d shows that WT mice responded robustly to both visible and NIR light. Quantitative analysis showed that the average anticipatory lick rate in NIR-stimulated rd1 mice was comparable with that of visible-light-stimulated WT mice (Extended Data Fig. 1e). Furthermore, we evaluated lick rate across various light intensities and found that anticipatory licking increased with NIR intensity in implanted rd1 mice, reaching levels similar to visible-light-driven behaviour in WT controls (Extended Data Fig. 1f). These results demonstrate that the NIR-perceptive artificial retina enables behaviourally relevant NIR vision while preserving the normal visual behaviour of sighted animals.

## Conclusion

We have reported an artificial retina capable of extending visual perception into the NIR spectrum. Our device integrates NIR-sensitive phototransistor arrays, an ultrathin NIR-transmission filter and soft 3D LM electrodes, allowing effective stimulation of retinal neurons under NIR illumination. The integration of NIR-sensitive phototransistors and 3D LM electrodes provides effective charge injection while minimizing tissue damage, owing to the electrode's low Young's modulus. The combination allows the selective stimulation of RGCs in a less mechanically invasive way compared with conventional rigid, solid-based 3D

electrodes<sup>23,24</sup>, making our device suitable for epiretinal implantation. The ultrathin NIR-transmission filter effectively blocks visible light while transmitting NIR light, enabling the device to function without interfering with normal vision. Ex vivo experiments demonstrate that our device can elicit retinal signals in healthy and blind retinas, suggesting its potential in restoring vision. Cortical recordings and behavioural tests of mice implanted with the artificial retina indicate perception of both visible and NIR light, suggesting that the artificial retina could restore or supplement vision as a visual prosthetic, or be used for therapeutic interventions.

The primary application of the NIR-perceptive artificial retina is supplementing vision in patients with photoreceptor degenerative blindness. For example, in patients with advanced retinitis pigmentosa (that is, intact inner retina but with little or no rod/cone function), our implant could provide a NIR-based visual channel while preserving the natural vision that remains. By using an NIR illumination source in dark environments, a blind user could perceive surroundings by means of the implant, effectively granting vision in conditions where normal sight is minimal.

To enhance practicality in real-world environments, multilayer-based optical filtering strategies (such as frequency filtering, bandwidth tuning and angle selectivity), can be employed to suppress background NIR noise from solar radiation and artificial sources. These filters, composed of alternating layers of  $\text{SiO}_2$  and amorphous silicon, can achieve selective transmittance based on wavelength and incident angle (Extended Data Fig. 2; further details on the filter design are provided in the Methods). By implementing these strategies, signal specificity under complex lighting conditions can be improved and environmental interference reduced.

Although our current device is designed to detect NIR light, it could be adapted to sense other wavelengths by changing the channel material of the phototransistor or modifying the filter structure. For example, the same mechanism could be used to stimulate the retina if the phototransistor was designed to absorb ultraviolet light. This adaptability opens possibilities for creating devices that can detect a range of wavelengths, from ultraviolet to visible to NIR, for various applications. Future work will focus on further miniaturizing the device to enhance its structural flexibility and reduce power consumption. This can be achieved by substituting the silicon channels in the phototransistors with flexible, highly NIR-sensitive semiconducting nanomaterials. In addition, long-term in vivo studies are needed to assess the biocompatibility and stability of the device over extended periods.

## Methods

**Fabrication of Si phototransistor arrays for the artificial retina**  
First, an array of single-crystalline Si, which serves as the channel of the transistor, was photolithographically patterned using a negative photoresist (SU-8, MicroChem) on a silicon-on-insulator (SOI) wafer ( $1.5 \mu\text{m}$  Si on  $3 \mu\text{m}$  buried oxide, Soitec, France). The Si channels were etched with an RIE system with tetrafluoromethane ( $\text{CF}_4$ ) plasma ( $\text{CF}_4$  40 sccm/ $\text{O}_2$  4 sccm, 200 mTorr, 150 W/530 s) to complete the channel isolation process. Photoresist residue was subsequently removed through Piranha solution (15 min). To separate the Si channel from the SOI wafer, the buried oxide layer was etched in a 50% hydrogen fluoride solution (18 min). Next, the pattern of Si channels was transferred from an SOI wafer onto a thin and transparent polyimide film (thickness:  $8 \mu\text{m}$ ) using a polydimethylsiloxane stamp (Sylgard 184, 10:1 weight ratio of base and curing agent). Cr 5 nm/Au 100 nm were deposited using an electron-beam evaporator and were patterned photolithographically to form source, drain electrodes and interconnects. Subsequently, a  $1.3\text{-}\mu\text{m}$ -thick silicon dioxide ( $\text{SiO}_2$ ) layer was deposited at  $150^\circ\text{C}$  using plasma-enhanced chemical vapour deposition (PECVD) and patterned photolithographically to serve as a dielectric layer. For the patterning of the gate electrode, a sacrificial layer (LOR 3 A photoresist,

Kayaku) was spin-coated on the substrate and was patterned photolithographically. Then ITO was deposited with a thickness of 150 nm at room temperature by radio frequency magnetron sputtering and was immersed in mr-Rem 700 (Lift-off solution, Micro resist technology) at 60 °C for 30 minutes to melt the sacrificial layer. As a biocompatible encapsulation layer, a 1- $\mu\text{m}$ -thick layer of parylene C was deposited. The local areas of these drain pads were opened by dry RIE etching ( $\text{O}_2$  40 sccm, 100 W/240 s) as the sites for printing the stimulation electrodes. Before the formation of 3D EGaIn electrodes, a 30-nm-thick layer of Pt was deposited on the opened areas with an electron-beam evaporator to prevent gold penetration into the EGaIn. After this step, the device was detached from the Si substrate and flipped to face the bottom side of the substrate (opposite the phototransistor side). Then PECVD was used to deposit an NIR-transmission filter on the bottom side of the PI film. The NIR-transmission filter comprised alternating layers of ultrathin a-Si and  $\text{SiO}_2$ , with a total thickness of 360 nm. After deposition, the filter was photolithographically patterned using dry RIE etching with tetrafluoromethane ( $\text{CF}_4$ ) plasma ( $\text{CF}_4$  40 sccm/ $\text{O}_2$  4 sccm, 200 mTorr, 150 W/135 s). Subsequently, the device was flipped again, and 3D protruding micropillars of LM (that is, EGaIn) were directly printed on the open surface of the drain pads using a capillary nozzle to form the stimulation electrodes. After coating a parylene C layer (thickness: 1  $\mu\text{m}$ ) on the entire sidewall of 3D LM pillars, their tips were locally opened using an anisotropic RIE process to selectively deposit Pt nanoclusters on the tips.

### Optical properties of the NIR-transmission filter

Considering the structure of our artificial retina, we designed a thin NIR-transmission filter (thickness: 360 nm) that can effectively cutoff transmission of the visible-light range and transmit only NIR light. Supplementary Fig. 16a illustrates the artificial retina when illuminated with incident light, and Supplementary Fig. 16b shows the magnified schematic of a single pixel of the phototransistor; specifically the photoactive region. As depicted in Supplementary Fig. 16b, the only membrane that light passes through to reach the Si channel is an 8- $\mu\text{m}$ -thick PI film. We therefore designed a filter for the optimal cutoff of visible light and transmittance of NIR light as light passes through this PI film and reaches the Si channel. As shown in the schematic in Supplementary Fig. 17a, the optical filter consists of seven alternating layers of a-Si and  $\text{SiO}_2$ . Supplementary Fig. 17b shows a cross-sectional SEM image of the NIR filter. The thickness of the layers are optimized for high transmissive efficiency, using stacks of the ' $H/2LH/2$ ' unit of antireflection coatings, based on Herpin's equivalent index<sup>25</sup>, where  $H$  and  $L$  denote the high and low refractive index materials with a quarter-wavelength thickness, respectively (that is,  $H = \lambda_c/4n_H$  and  $L = \lambda_c/4n_L$ ;  $\lambda_c$  = critical wavelength;  $n_H$  = refractive index of the high-index layer;  $n_L$  = refractive index of the low-index layer). The refractive indices used in our studies are shown in Supplementary Fig. 18. Considering the refractive indices and the critical wavelength (520 nm), we set  $H$ , the thickness of the high refractive index material (that is, a-Si), as 50 nm and  $L$ , the thickness of the low refractive index material (that is,  $\text{SiO}_2$ ), as 75 nm. This design enabled effective blocking of light transmission from 440 nm to 600 nm. Moreover, the a-Si layer within the filter absorbed incident visible light due to its intrinsic absorptivity, resulting in near-complete blocking of visible-light transmission (Supplementary Fig. 19). For the transmission spectra shown in Supplementary Fig. 19, a quartz substrate was used. Detailed explanations of the fabrication and simulations regarding the optical filter are in Methods and the Supplementary Information. Simulations of absorptivity spectra for the Si layer only are shown in Supplementary Fig. 20. The results indicate that the NIR filter effectively blocks visible-light transmission while allowing NIR-light transmission, which thus maintains the absorptivity in the NIR range of the Si channels comprising the phototransistors.

### Fabrication of NIR-transmission filters

A substrate coated with SU-8, ITO and  $\text{SiO}_2$  was prepared. The design configuration of NIR-transparent optical filters consisted of a multilayer with alternating layers of a-Si and  $\text{SiO}_2$ . The deposition of all a-Si and  $\text{SiO}_2$  layers was performed using PECV; HiDep-SC, BMR Technology). The process began with the deposition of the first a-Si layer, followed by the deposition of the  $\text{SiO}_2$  layer. This sequence was repeated until the final multilayer was achieved.

### Multilayer NIR-filter design and simulation

To suppress background NIR noise originating from environmental sources such as solar radiation and artificial lighting, we designed multilayer optical filters using alternating layers of  $\text{SiO}_2$  and a-Si based on three approaches: (1) frequency filtering; (2) bandwidth filtering; and (3) angle filtering, which are illustrated in Extended Data Fig. 2a. These filters were engineered to selectively transmit specific NIR wavelengths or angles of incidence, thereby improving spectral fidelity and minimizing noise in complex illumination environments.

Each multilayer structure was constructed by alternating 30-nm-thick layers of  $\text{SiO}_2$  (denoted '0') and a-Si (denoted as '1'), with binary sequences defining the transmission characteristics of each design as shown in Extended Data Fig. 2b. Optical simulations were conducted assuming an infinitely thick  $\text{SiO}_2$  glass substrate to eliminate interference effects from substrate reflections and boundaries. The optical constants of a-Si and  $\text{SiO}_2$  are shown in Supplementary Fig. 21.

Three distinct filtering strategies were employed.

- (1) Wavelength-selective filtering: designs (i)–(iii) were optimized to transmit narrow spectral bands centred at 950 nm, 1,000 nm and 1,050 nm, respectively. The simulated transmission spectra of these filters revealed sharp peaks at the target wavelengths (Extended Data Fig. 2c), demonstrating effective frequency discrimination against broadband NIR background light.
- (2) Bandwidth tuning: designs (iv)–(vi) were developed to modulate the full-width at half-maximum (FWHM) of the transmission peaks at a fixed centre wavelength (950 nm). By adjusting the binary layer sequence, FWHM values of 30 nm, 135 nm and 215 nm were achieved (Extended Data Fig. 2d), enabling tunable spectral bandwidths to accommodate different application needs.
- (3) Angle-dependent filtering: design (vii) was engineered to exhibit strong angle selectivity, reducing transmittance for oblique incidence angles. As shown in Extended Data Fig. 2e, the filter maintained a high transmittance ( $\sim 0.99$ ) at 980 nm under normal incidence, but transmittance dropped substantially for both transverse electric and transverse magnetic polarizations with increasing incident angle, reaching  $\sim 0.5$  at 10° (transverse electric) and 6° (transverse magnetic). This feature helps to suppress off-axis NIR interference and enhances signal-to-noise ratio during device operation.

All optical simulations were performed using a transfer matrix method implemented in MATLAB (MathWorks, USA), assuming non-dispersive refractive indices for  $\text{SiO}_2$  and a-Si. These filtering strategies were experimentally validated by means of transmission spectroscopy and implemented in the final device fabrication to enhance real-world performance.

### Fabrication of 3D LM electrodes

The key steps in the fabrication of the 3D LM electrodes are as follows.

- (1) Direct printing of 3D EGaIn electrodes: the direct printing system consisted of a capillary nozzle connected to an ink reservoir; a pneumatic pressure controller and a six-axis stage (H-820 6-Axis Hexapod, Physik Instrumente) with automatic

movements in the  $x$ ,  $y$  and  $z$  axes; two tilting axes in the  $x$  and  $y$  axes; and rotation in the  $x$ - $y$  plane. First, a pipette puller (P-1000, Sutter Instrument) was used to make a glass capillary (Sutter Instrument) as a nozzle with inner diameters of 5–50  $\mu\text{m}$ . Then the nozzle was mounted onto a syringe-type reservoir, and a substrate was placed on the six-axis stage. All of the LM printing steps were recorded by a microscope camera (QImaging MicroPublisher 5.0 with real-time viewing, Teledyne Photometrics) to control the nozzle relative to the substrate using the six-axis stage during the printing process. The distance between the tip of the nozzle and the substrate was controlled to be in the range of 2–16  $\mu\text{m}$  according to the diameter of the nozzle, and pneumatic pressure ( $\sim 50$  psi) was applied to deliver EGaIn ink (75.5% gallium and 24.5% indium alloy by weight; Changsha Santech Materials) through the nozzle onto the substrate. After we controlled the  $z$  axis of the six-axis stage to make contact between EGaIn and the opened area of the drain electrode, the ink was directly printed in a circular shape on the top surface of the drain to exhibit a thicker base of the 3D micropillar for structural stability. By adjusting the printing motion along the  $z$  axis at a velocity in the range 1–500  $\mu\text{m s}^{-1}$ , the 3D pillar of EGaIn with a uniform diameter (except the circular base part) can be printed. On exposure to air, EGaIn instantly forms a thin solid layer ( $\sim 1$  nm) of gallium oxide on its surface under atmospheric oxygen levels to maintain its vertical 3D structure. This oxide skin is thin enough to avoid substantially damaging the cellular interfaces, and it is solid enough to maintain its 3D shape against gravity and surface tension.

- (2) Selective opening of 3D electrode tips: after the printing of the 3D pristine EGaIn electrodes, additional parylene C (thickness, 1  $\mu\text{m}$ ) was deposited on the entire device, including the 3D electrodes for the passivation of their sidewalls. Only their tips were selectively opened using anisotropic  $\text{O}_2$  RIE (100 W/240 s). In addition to the encapsulation layer of the sidewalls of the 3D micropillars, the additional parylene C layer served as a protective layer of the first parylene C encapsulation layer.
- (3) Deposition of Pt nanoclusters: to prepare 50 ml of an electroplating solution, we mixed 50 ml of deionized water, 10 mg of lead acetate trihydrate (Sigma-Aldrich) and 0.5 g of platinum tetrachloride (Sigma-Aldrich) at room temperature. This electroplating solution was stirred for 20 min by ultrasonic vibration. The electroplating was performed by ion transfer between the cathode and anode in the Pt electroplating solution. After mounting the device to a multichannel recording interface (MZ-60, Tucker-Davis Technologies), a cathode (the 3D pristine EGaIn microelectrode that is to be electroplated) and an anode (Ti/Pt electrode) were immersed in this electroplating solution, and each electrode was connected to a source meter (Keithley 2400, Tektronix). An electrical current of 0.1 mA was applied for 60 s to generate the electroplating reaction. Owing to potential variations in current under light exposure, we performed the electroplating of Pt nanoclusters in the dark.
- (4) Rinsing process of the artificial retina: before implantation of the device, the artificial retina was rinsed by gently immersing the device in 70% ethanol solution (15 min) and deionized water (15 min) followed by ultraviolet exposure (30 min).

### Ex vivo animal experiments

The retinas of WT (C57BL/6 J, Japan SLC) and rd1 (C3H/HeNcrIori, Japan SLC) mice were explanted. A small piece ( $\sim 4 \times 4$  mm) of retina was isolated and transferred to the artificial retina with PBS media by placing ganglion cell side down to face the device and maintained at 37 °C with a heating pad. The animal was sacrificed immediately by cervical dislocation after the extraction. Immediately before implanting this device into the retina, the device sample was frozen to turn the

liquid-phase EGaIn into a solid by cooling it below the melting point of EGaIn,  $\sim 15.7$  °C and placing in cold storage. The pillars of 3D LM electrodes then returned to a liquid phase and did not collapse after being implanted into the retina. Neural responses of the mouse retina were generated by operating a phototransistor array with a pulsed bias of 3 V to  $V_D$  with a pulse duration of 1 ms and frequency of 10 Hz, and a d.c. bias of  $-20$  V for  $V_G$ . Electrophysiological recordings were conducted by multielectrode array recording and multichannel stimulation (PZ5 and Subject Interface, Tucker-Davis Technologies, USA) and a data processor with a real-time controller (RZ2 BioAmp Processor, Tucker-Davis Technologies, USA). We recorded OEP and EEP signals at a 25-kHz sampling rate using a 300-Hz low-pass and 3-kHz high-pass filter. The experimental data were processed by applying a bandpass filter with MATLAB (MathWorks, USA). All animal experimental procedures were conducted based on the guidelines and were approved by the Institute of Animal Care and Use Committee of Yonsei University. (IACUC-202202-1415-04, Yonsei IACUC, Korea).

### In vivo animal experiment for the retinal stimulation

WT (C57BL/6NcrIori mice; 8–12 weeks old) and rd1 mice (C3H/HeNcrIori mice; 8–12 weeks old) were used in this study. All mice were housed under a 12-hour light/dark cycle at an ambient temperature of 22 °C and a relative humidity of 50–60%, with food and water provided ad libitum. The mouse was fixed in a stereotaxic frame. A NIR-perceptive artificial retina, integrated with a  $6 \times 6$  array of Si phototransistors (pixel pitch: 500  $\mu\text{m}$  and device dimension of 1 mm in width), was implanted to the innermost retinal surface of the rd1 mouse, with external device interconnections. The recording lines were connected to the glass pad with interconnect electrodes, patterned with photolithography, and wet etching after deposition of Cr/Au (10/100 nm) by an e-beam evaporator. The interconnect pad was inserted into the multielectrode array recorder with a multichannel stimulator (PZ5 and Subject Interface, Tucker-Davis Technologies, USA) and a data processor with a real-time controller (RZ2 BioAmp Processor, Tucker-Davis Technologies, USA). The multichannel experimental data of spike signal and firing rate were obtained and exported by analysis software (Synapse Suite, Tucker-Davis Technologies, USA). Then the data were processed and mapped with MATLAB (MathWorks, USA).

A commercial blue (wavelength: 470 nm) and NIR (wavelength: 900 nm) LED was fixed in front of the eyeball and delivered light for the optical stimulation. Illumination of visible light (wavelength of 470 nm) or NIR light (wavelength of 900 nm) was applied to the fundus of the mouse eye. Lensectomy was performed to conformally attach the NIR-perceptive artificial retina onto the surface of the retina. The artificial retina applied monophasic electrical pulses (5  $\mu\text{A}$ , 1 ms and 10 Hz) upon NIR-light exposure (duration: 0.5 s) to the retinal ganglion cells by means of 36 pixels of 3D LM electrodes. Typical sessions lasted 3 h, from implantation to electrophysiological signal recordings. To record the neural responses by the stimulations, parylene C insulated commercial tungsten microelectrodes ( $\sim 1$  M $\Omega$  at 1 kHz, 100  $\mu\text{m}$  diameter) were inserted into the primary visual cortex (at the coordinates anteroposterior,  $-3.0$  mm; mediolateral,  $+2.5$  mm; dorsoventral, 1 mm). The neural signal was filtered between 0.3 kHz and 5 kHz and sampled at 25 kHz. Animal experiments were conducted based on the guidelines of the Institute of Animal Care and Use Committee of Yonsei University. (IACUC-202312-1774-01, Yonsei IACUC, Korea).

### In vivo behavioural tests

WT mice and Rd1 mice were handled daily and received  $\sim 0.5$ –1 ml of water per session, until body weight reached  $\sim 80\%$  of the ad libitum weight (typically within 5–7 days). Health status and weight were monitored daily. Before starting behavioural evaluation, mice were progressively habituated to the experimental set-up, including head fixation and enclosure within a 'body' tube. Enclosure of the mouse body within a cylindrical acrylic tube was found to maximize animal comfort during

head fixation. Eyes were dilated with atropine 0.5% 15 min before behavioural evaluation. Rd1 experiments were performed in the dark. NIR experiments in WT mice were performed in ambient light. Visible-light experiments in WT mice were performed in the dark. Mice performed a voluntary action NIR-detection task by licking a waterspout (18 G needle, 5 mm from mouth) in response to full-field, 200-ms stimulation of one eye (900-nm NIR light). Water (~7 µl) was automatically dispensed 500 ms after light onset, through a calibrated gravity water system gated with a solenoid pinch valve. Intervals between trials ranged from 10 s to 30 s. Training lasted four days for NIR light and for visible light. Typical sessions lasted ~40 min. To assess the impact of the light cue, lick rates were calculated after stimulus onset but before water valve opening. Spontaneous background lick rates (1-s time window before stimulus onset) were subtracted from stimulus-driven lick rates. For Z scores, the mean and standard deviation of a 500-ms background time interval was used. An Arduino Uno board provided control of the behavioural protocol, including lick detection, water valve opening and variation of NIR-stimulus intensities.

### Reporting summary

Further information on research design is available in the Nature Portfolio Reporting Summary linked to this article.

### Data availability

The data regarding the characterization of the NIR-perceptive artificial retina and animal experiments are available via figshare at <https://doi.org/10.6084/m9.figshare.30631124> (ref. 26). The raw neural datasets generated during this study are available from the corresponding authors upon reasonable request. Source data are provided with this paper.

### Code availability

The source codes for MATLAB are available via figshare at <https://doi.org/10.6084/m9.figshare.30631124> (ref. 26).

### References

- Seo, H. et al. Smart contact lenses as wearable ophthalmic devices for disease monitoring and health management. *Chem. Rev.* **123**, 11488–11558 (2023).
- Mathieson, K. et al. Photovoltaic retinal prosthesis with high pixel density. *Nat. Photon.* **6**, 391–397 (2012).
- Chenais, N. A. L., Airaghi Leccardi, M. J. I. & Ghezzi, D. Photovoltaic retinal prosthesis restores high-resolution responses to single-pixel stimulation in blind retinas. *Commun. Mater.* **2**, 1–16 (2021).
- Choi, C. et al. Human eye-inspired soft optoelectronic device using high-density MoS<sub>2</sub>-graphene curved image sensor array. *Nat. Commun.* **8**, 1664 (2017).
- Zhao, S. et al. Tracking neural activity from the same cells during the entire adult life of mice. *Nat. Neurosci.* **26**, 696–710 (2023).
- Ma, Y. et al. Mammalian near-infrared image vision through injectable and self-powered retinal nanoantennae. *Cell* **177**, 243–255 (2019).
- Nelidova, D. et al. Restoring light sensitivity using tunable near-infrared sensors. *Science* **368**, 1108–1113 (2020).
- Palanker, D., Le Mer, Y., Mohand-Said, S. & Sahel, J. A. Simultaneous perception of prosthetic and natural vision in AMD patients. *Nat. Commun.* **13**, 513 (2022).
- Jang, J., Kim, H., Song, Y. M. & Park, J.-U. Implantation of electronic visual prosthesis for blindness restoration. *Opt. Mater. Express* **9**, 3878–3894 (2019).
- Cho, Y. H., Park, Y.-G., Kim, S. & Park, J.-U. 3D electrodes for bioelectronics. *Adv. Mater.* **33**, 2005805 (2021).
- ISO 10993-5:2009(en) biological evaluation of medical devices—part 5: tests for in vitro cytotoxicity. *ISO OBP* <https://www.iso.org/obp/ui/en/#iso:std:iso:10993:-5:ed-3:v1:en> (2009).

- Giménez, M. C. et al. Effects of near-infrared light on well-being and health in human subjects with mild sleep-related complaints: a double-blind, randomized, placebo-controlled study. *Biology* **12**, 60 (2022).
- Yuk, H., Lu, B. & Zhao, X. Hydrogel bioelectronics. *Chem. Soc. Rev.* **48**, 1642–1667 (2019).
- Kim, S. et al. Materials and structural designs for neural interfaces. *ACS Appl. Electron. Mater.* **5**, 1926–1946 (2023).
- Lee, S. et al. Electrophysiological analysis of retinal organoid development using 3D microelectrodes of liquid metals. *Adv. Mater.* **36**, 2404428 (2024).
- Park, Y.-G. et al. High-resolution 3D printing for electronics. *Adv. Sci.* **9**, 2104623 (2022).
- Chung, W. G. et al. Ga-based liquid metals: versatile and biocompatible solutions for next-generation bioelectronics. *Adv. Funct. Mater.* **34**, 307990 (2024).
- Jones, I. L., Warner, M. & Stevens, J. D. Mathematical modelling of the elastic properties of retina: a determination of Young's modulus. *Eye* **6**, 556–559 (1992).
- Shin, H. et al. Recent progress on wearable point-of-care devices for ocular systems. *Lab Chip* **21**, 1269–1286 (2021).
- Lee, J. et al. Engineering implantable bioelectronics for electrophysiological monitoring in preclinical animal models. *Adv. Eng. Mater.* **26**, 2400499 (2024).
- Chung, W. G. et al. Liquid-metal-based three-dimensional micro-electrode arrays integrated with implantable ultrathin retinal prosthesis for vision restoration. *Nat. Nanotechnol.* **19**, 688–697 (2024).
- Do, M. T. et al. Submicrometer 3D structures fabrication enabled by one-photon absorption direct laser writing. *Opt. Express* **21**, 20964–20973 (2013).
- Davidsen, R. S., Hemanth, S., Keller, S. S., Bek, T. & Hansen, O. Evaluation of the capacitive behavior of 3D carbon electrodes for sub-retinal photovoltaic prosthesis. *Micro Nano Eng.* **2**, 110–116 (2019).
- Bendali, A. et al. Synthetic 3D diamond-based electrodes for flexible retinal neuroprostheses: model, production and in vivo biocompatibility. *Biomaterials* **67**, 73–83 (2015).
- Ji, C. et al. Decorative near-infrared transmission filters featuring high-efficiency and angular-insensitivity employing 1D photonic crystals. *Nano Res.* **12**, 543–548 (2019).
- Chung, W. G. et al. Dataset for 'An implantable epiretinal device for near-infrared light perception'. *figshare* <https://doi.org/10.6084/m9.figshare.30631124> (2026).

### Acknowledgements

This work was supported by the Ministry of Science & ICT (MSIT), the Ministry of Trade, Industry and Energy (MOTIE), the Ministry of Health & Welfare, and the Ministry of Food and Drug Safety of Korea through the National Research Foundation (RS-2023-NR077138, RS-2024-00464032, RS-2025-16063568, RS-2025-18362970); STEAM Research Program (RS-2024-00460364); ERC Program (RS-2024-00406240); Basic Science Research Program (RS-2023-00207966); Korean ARPA-H Project (RS-2025-25455885) and Technology Innovation Program (RS-2025-08672969). This work was also funded by the Korea Institute of Science and Technology (KIST) Institutional Program (2E33191 and 2E33190) and the Institute for Basic Science (IBS-R026-D1). W.G.C. also thanks the Sejong Science Fellowship (RS-2025-00514998).

### Author contributions

W.G.C. carried out the experiments, analysed the data and wrote the paper. I.J. wrote the paper and characterized the 3D liquid metal electrodes. E.-J.L. performed the simulation of the NIR-transmission filters. G.C. and M.S.C. performed the implantation of the NIR-perceptive artificial retinas during in vivo experiments. S.L., S.H.A. and E.K. conducted ex vivo experiments, and S.K. performed the printing of

the 3D EGIn electrodes. H.J. and J.L. performed the biocompatibility tests. S.H.B. oversaw animal experiments and revised the paper. S.-K.K. oversaw NIR-transmission characterizations and revised the paper. J.-U.P. oversaw all the research phases and revised the paper. All authors participated in discussions and commented on the paper.

### Competing interests

The authors declare no competing interests.

### Additional information

**Extended data** is available for this paper at <https://doi.org/10.1038/s41928-026-01601-8>.

**Supplementary information** The online version contains supplementary material available at <https://doi.org/10.1038/s41928-026-01601-8>.

**Correspondence and requests for materials** should be addressed to Suk Ho Byeon, Sun-Kyung Kim or Jang-Ung Park.

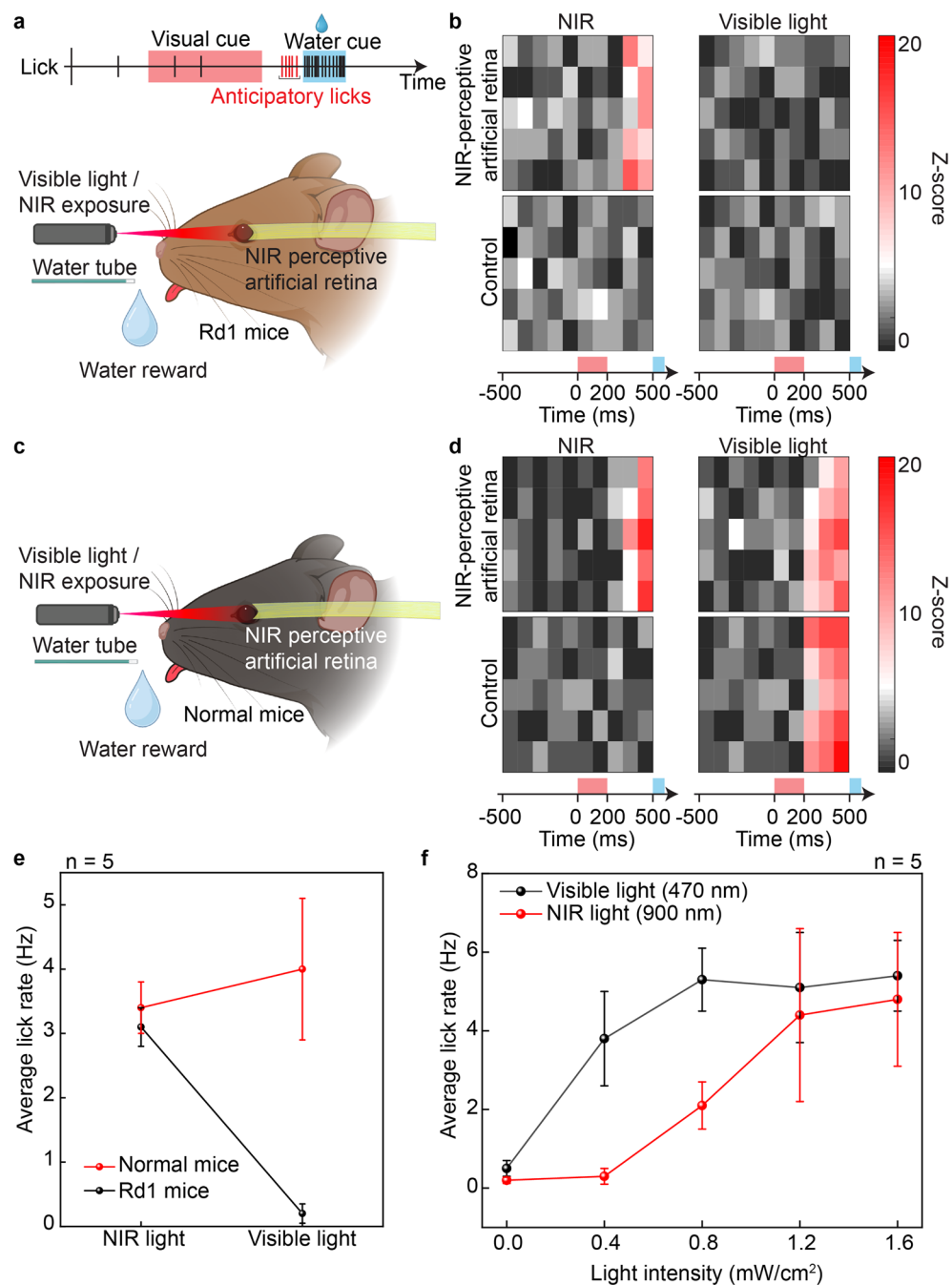
**Peer review information** *Nature Electronics* thanks Chao Ping Chen, Kevin Wu and the other, anonymous, reviewer(s) for their contribution to the peer review of this work.

**Reprints and permissions information** is available at [www.nature.com/reprints](http://www.nature.com/reprints).

**Publisher's note** Springer Nature remains neutral with regard to jurisdictional claims in published maps and institutional affiliations.

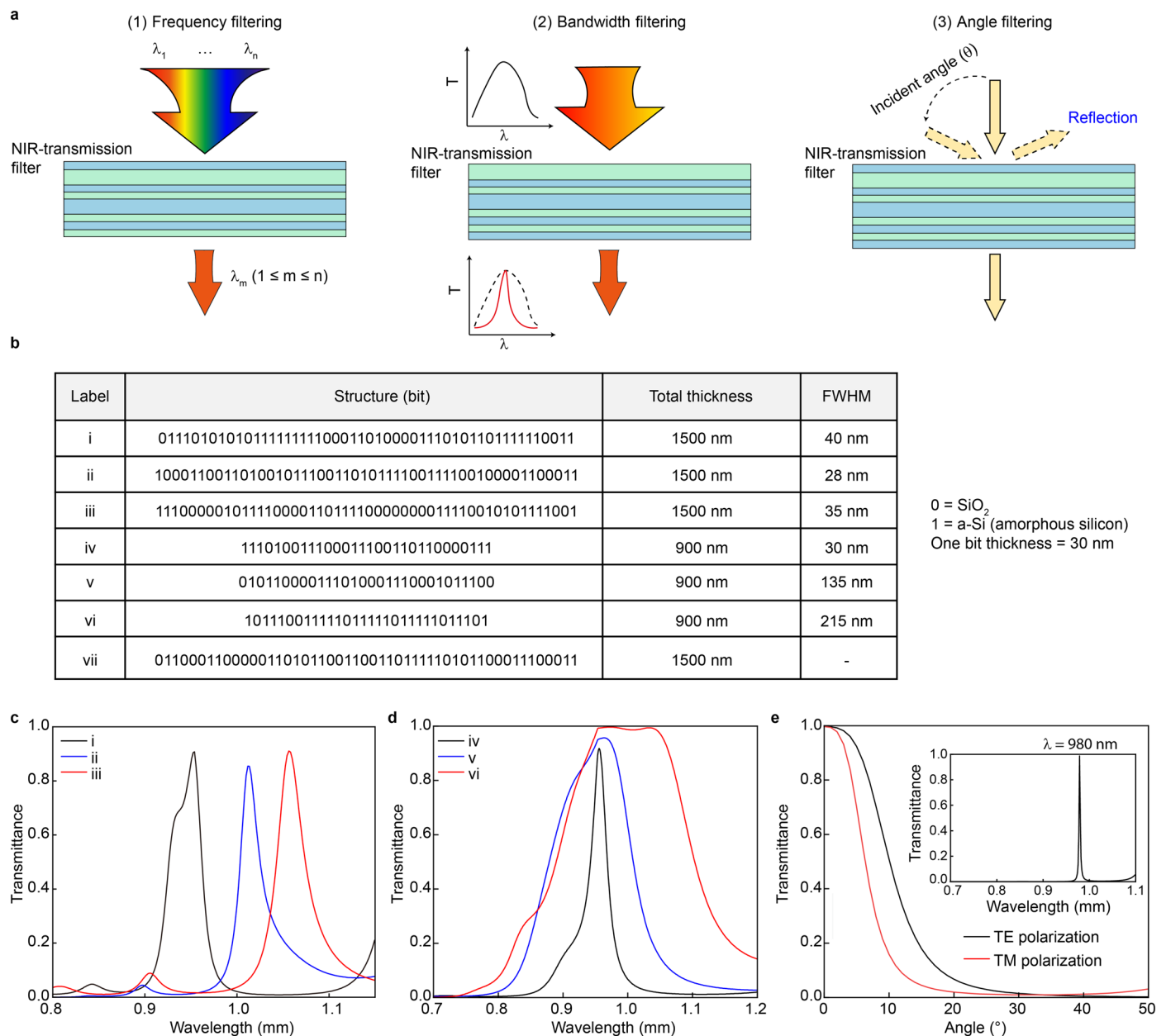
**Open Access** This article is licensed under a Creative Commons Attribution 4.0 International License, which permits use, sharing, adaptation, distribution and reproduction in any medium or format, as long as you give appropriate credit to the original author(s) and the source, provide a link to the Creative Commons licence, and indicate if changes were made. The images or other third party material in this article are included in the article's Creative Commons licence, unless indicated otherwise in a credit line to the material. If material is not included in the article's Creative Commons licence and your intended use is not permitted by statutory regulation or exceeds the permitted use, you will need to obtain permission directly from the copyright holder. To view a copy of this licence, visit <http://creativecommons.org/licenses/by/4.0/>.

© The Author(s) 2026



**Extended Data Fig. 1 | Visible and NIR light-guided behavior.** **a**, Schematic of the behavioral setup for rd1 mice implanted with the NIR-perceptive artificial retina. NIR (900 nm) or visible light (470 nm) served as a cue preceding water reward delivery. Anticipatory licking was measured before water delivery. **b**, Heat maps showing time-aligned lick activity (z-scored) in response to NIR and visible light cues in rd1 mice with or without the NIR-perceptive artificial retina ( $n = 5$  biologically independent mice per group). **c**, Behavioral setup for wild-type (normal) mice implanted with the same device. **d**, Heat maps of lick behavior in response to light cues in normal mice, showing that the artificial retina enables anticipatory licking upon NIR exposure, while control mice respond only to

visible light. **e**, Average anticipatory lick rates for rd1 and normal mice under NIR and visible light stimulation. Rd1 mice with the NIR-perceptive retina respond preferentially to NIR cues, while normal mice respond to both. Data are mean  $\pm$  S.D. with  $n = 5$  biologically independent mice. **f**, Lick rate as a function of light intensity for NIR and visible light in normal mice. Data are mean  $\pm$  S.D. with  $n = 5$  biologically independent mice. Both types of light produced graded increases in lick rate, indicating effective cue association and perceptual integration. Mouse illustrations in **a** and **c** created in BioRender; Chung, W. <https://biorender.com/lji5rqi> (2026).



### Extended Data Fig. 2 | Multilayer NIR filter design for practical applications.

**a**, Optical filtering strategies based on multilayers. Schematics of three filtering mechanisms addressing (1) frequency, (2) bandwidth, and (3) angle selectivity. **b**, Structural parameters of the NIR filters (i-vii). Each filter is represented by a binary layer sequence, where 0 indicates a 30 nm SiO<sub>2</sub> layer and 1 indicates to a 30 nm a-Si layer. All multilayer designs were computed assuming an infinite-thickness SiO<sub>2</sub> glass substrate to effectively analysis characteristics from any substrate boundary effects. **c**, Transmission spectra of the filters (i, ii, iii), each

tuned to a different central wavelength at 950, 1000, and 1050 nm, respectively. **d**, Transmission spectra of the filters (iv, v, vi) designed for bandwidth control at a fixed centre wavelength of 950 nm, showing adjustable FWHM values of 30, 135, and 210 nm, respectively. **e**, Transmittance spectra of angle-selective filter (vii) at 980 nm for TE and TM polarization with varying incident angles ( $\theta$ ). The filter (vii) achieves maximum transmittance at normal incidence, and its transmittance for both polarizations drops below 0.5 when the incident angle exceeds 10°.

## Reporting Summary

Nature Portfolio wishes to improve the reproducibility of the work that we publish. This form provides structure for consistency and transparency in reporting. For further information on Nature Portfolio policies, see our [Editorial Policies](#) and the [Editorial Policy Checklist](#).

### Statistics

For all statistical analyses, confirm that the following items are present in the figure legend, table legend, main text, or Methods section.

n/a Confirmed

- The exact sample size ( $n$ ) for each experimental group/condition, given as a discrete number and unit of measurement
- A statement on whether measurements were taken from distinct samples or whether the same sample was measured repeatedly
- The statistical test(s) used AND whether they are one- or two-sided  
*Only common tests should be described solely by name; describe more complex techniques in the Methods section.*
- A description of all covariates tested
- A description of any assumptions or corrections, such as tests of normality and adjustment for multiple comparisons
- A full description of the statistical parameters including central tendency (e.g. means) or other basic estimates (e.g. regression coefficient) AND variation (e.g. standard deviation) or associated estimates of uncertainty (e.g. confidence intervals)
- For null hypothesis testing, the test statistic (e.g.  $F$ ,  $t$ ,  $r$ ) with confidence intervals, effect sizes, degrees of freedom and  $P$  value noted  
*Give  $P$  values as exact values whenever suitable.*
- For Bayesian analysis, information on the choice of priors and Markov chain Monte Carlo settings
- For hierarchical and complex designs, identification of the appropriate level for tests and full reporting of outcomes
- Estimates of effect sizes (e.g. Cohen's  $d$ , Pearson's  $r$ ), indicating how they were calculated

*Our web collection on [statistics for biologists](#) contains articles on many of the points above.*

### Software and code

Policy information about [availability of computer code](#)

Data collection: Electrophysiological recordings of the ex-vivo retina and in-vivo experiments: Multi-electrode array recording and a data processor with a real-time controller (RZ2 BioAmp Processor, Tucker-Davis Technologies, USA)  
Microsoft Excel 2022

Data analysis: Bandpass filtering and spike detection was made by a custom code with MATLAB R2021a (MathWorks)  
Origin Pro 2022b (Origin Lab)

For manuscripts utilizing custom algorithms or software that are central to the research but not yet described in published literature, software must be made available to editors and reviewers. We strongly encourage code deposition in a community repository (e.g. GitHub). See the Nature Portfolio [guidelines for submitting code & software](#) for further information.

### Data

Policy information about [availability of data](#)

All manuscripts must include a [data availability statement](#). This statement should provide the following information, where applicable:

- Accession codes, unique identifiers, or web links for publicly available datasets
- A description of any restrictions on data availability
- For clinical datasets or third party data, please ensure that the statement adheres to our [policy](#)

Figshare dataset link:

## Research involving human participants, their data, or biological material

Policy information about studies with [human participants or human data](#). See also policy information about [sex, gender \(identity/presentation\), and sexual orientation](#) and [race, ethnicity and racism](#).

### Reporting on sex and gender

*Use the terms sex (biological attribute) and gender (shaped by social and cultural circumstances) carefully in order to avoid confusing both terms. Indicate if findings apply to only one sex or gender; describe whether sex and gender were considered in study design; whether sex and/or gender was determined based on self-reporting or assigned and methods used. Provide in the source data disaggregated sex and gender data, where this information has been collected, and if consent has been obtained for sharing of individual-level data; provide overall numbers in this Reporting Summary. Please state if this information has not been collected. Report sex- and gender-based analyses where performed, justify reasons for lack of sex- and gender-based analysis.*

### Reporting on race, ethnicity, or other socially relevant groupings

*Please specify the socially constructed or socially relevant categorization variable(s) used in your manuscript and explain why they were used. Please note that such variables should not be used as proxies for other socially constructed/relevant variables (for example, race or ethnicity should not be used as a proxy for socioeconomic status). Provide clear definitions of the relevant terms used, how they were provided (by the participants/respondents, the researchers, or third parties), and the method(s) used to classify people into the different categories (e.g. self-report, census or administrative data, social media data, etc.) Please provide details about how you controlled for confounding variables in your analyses.*

### Population characteristics

*Describe the covariate-relevant population characteristics of the human research participants (e.g. age, genotypic information, past and current diagnosis and treatment categories). If you filled out the behavioural & social sciences study design questions and have nothing to add here, write "See above."*

### Recruitment

*Describe how participants were recruited. Outline any potential self-selection bias or other biases that may be present and how these are likely to impact results.*

### Ethics oversight

*Identify the organization(s) that approved the study protocol.*

Note that full information on the approval of the study protocol must also be provided in the manuscript.

## Field-specific reporting

Please select the one below that is the best fit for your research. If you are not sure, read the appropriate sections before making your selection.

Life sciences  Behavioural & social sciences  Ecological, evolutionary & environmental sciences

For a reference copy of the document with all sections, see [nature.com/documents/nr-reporting-summary-flat.pdf](https://www.nature.com/documents/nr-reporting-summary-flat.pdf)

## Life sciences study design

All studies must disclose on these points even when the disclosure is negative.

Sample size

Data exclusions

Replication

Randomization

Blinding

## Reporting for specific materials, systems and methods

We require information from authors about some types of materials, experimental systems and methods used in many studies. Here, indicate whether each material, system or method listed is relevant to your study. If you are not sure if a list item applies to your research, read the appropriate section before selecting a response.

## Materials &amp; experimental systems

- n/a | Involved in the study
- Antibodies
- Eukaryotic cell lines
- Palaeontology and archaeology
- Animals and other organisms
- Clinical data
- Dual use research of concern
- Plants

## Methods

- n/a | Involved in the study
- ChIP-seq
- Flow cytometry
- MRI-based neuroimaging

## Antibodies

|                 |  |
|-----------------|--|
| Antibodies used | <p>The antibodies used in this study were as follows:<br/> anti-Iba1 (1:100, NB100-1028, Novus Biologicals, USA)<br/> anti-GFAP (1:100, ab7260, Abcam, UK)</p> <p>Donkey anti-rabbit IgG (1:1000, A-21207, Alexa Fluor® 594-conjugated, Thermo Fisher Scientific, USA)<br/> Donkey anti-goat IgG (1:1000, A-11055, Alexa Fluor® 488-conjugated, Thermo Fisher Scientific, USA).</p>  |
| Validation      | <p>All antibodies used in this study were obtained from the indicated commercial vendors, and the validations of each antibody are provided by the vendor on the products' webpage:<br/> anti-Iba1: <a href="https://www.novusbio.com/products/aif-1-iba1-antibody_nb100-1028">https://www.novusbio.com/products/aif-1-iba1-antibody_nb100-1028</a><br/> anti-GFAP: <a href="https://www.abcam.com/en-us/products/primary-antibodies/gfap-antibody-astrocyte-marker-ab7260">https://www.abcam.com/en-us/products/primary-antibodies/gfap-antibody-astrocyte-marker-ab7260</a></p> <p>Donkey anti-Rabbit IgG (H+L) Highly Cross-Adsorbed Secondary Antibody, Alexa Fluor™ 594: <a href="https://www.thermofisher.com/antibody/product/Donkey-anti-Rabbit-IgG-H-L-Highly-Cross-Adsorbed-Secondary-Antibody-Polyclonal/A-21207">https://www.thermofisher.com/antibody/product/Donkey-anti-Rabbit-IgG-H-L-Highly-Cross-Adsorbed-Secondary-Antibody-Polyclonal/A-21207</a><br/> Donkey anti-Goat IgG (H+L) Highly Cross-Adsorbed Secondary Antibody, Alexa Fluor™ Plus 488: <a href="https://www.thermofisher.com/antibody/product/Donkey-anti-Goat-IgG-H-L-Cross-Adsorbed-Secondary-Antibody-Polyclonal/A-11055">https://www.thermofisher.com/antibody/product/Donkey-anti-Goat-IgG-H-L-Cross-Adsorbed-Secondary-Antibody-Polyclonal/A-11055</a></p> |

## Eukaryotic cell lines

Policy information about [cell lines and Sex and Gender in Research](#)

|  |  |
|--|--|
| Cell line source(s)  | ARPE-19 was obtained from ATCC.  |
| Authentication   | The authentication of cell lines performed by ATCC can be found at <a href="https://www.atcc.org/api/pdf/product-sheet?id=CRL-2302">https://www.atcc.org/api/pdf/product-sheet?id=CRL-2302</a> . |
| Mycoplasma contamination   | All cell lines tested negative for mycoplasma.   |
| Commonly misidentified lines<br>(See <a href="#">ICLAC</a> register) | No commonly misidentified cell lines were used.  |

## Animals and other research organisms

Policy information about [studies involving animals; ARRIVE guidelines](#) recommended for reporting animal research, and [Sex and Gender in Research](#)

|                         |  |
|-------------------------|--|
| Laboratory animals      | Wild-type mice : Male, C57BL/6J, 8-weeks old; Rd1 mice : Male, C3H/, 8-weeks old   |
| Wild animals            | n/a  |
| Reporting on sex        | This study involved only male for both wild-type and rd1 mice to exclude sex-related variations.   |
| Field-collected samples | n/a  |
| Ethics oversight        | All of the experimental procedures performed on the animals were conducted based on the guidelines and were approved by the Institute of Animal Care and Use Committee of Yonsei University. |

Note that full information on the approval of the study protocol must also be provided in the manuscript.

## Plants

|                       |   |
|-----------------------|---|
| Seed stocks           | Report on the source of all seed stocks or other plant material used. If applicable, state the seed stock centre and catalogue number. If plant specimens were collected from the field, describe the collection location, date and sampling procedures.  |
| Novel plant genotypes | Describe the methods by which all novel plant genotypes were produced. This includes those generated by transgenic approaches, gene editing, chemical/radiation-based mutagenesis and hybridization. For transgenic lines, describe the transformation method, the number of independent lines analyzed and the generation upon which experiments were performed. For gene-edited lines, describe the editor used, the endogenous sequence targeted for editing, the targeting guide RNA sequence (if applicable) and how the editor was applied. |
| Authentication        | Describe any authentication procedures for each seed stock used or novel genotype generated. Describe any experiments used to assess the effect of a mutation and, where applicable, how potential secondary effects (e.g. second site T-DNA insertions, mosaicism, off-target gene editing) were examined.   |

## Flow Cytometry

### Plots

Confirm that:

- The axis labels state the marker and fluorochrome used (e.g. CD4-FITC).
- The axis scales are clearly visible. Include numbers along axes only for bottom left plot of group (a 'group' is an analysis of identical markers).
- All plots are contour plots with outliers or pseudocolor plots.
- A numerical value for number of cells or percentage (with statistics) is provided.

### Methodology

|                           |  |
|---------------------------|--|
| Sample preparation        | The artificial retina device and PI film were each cut into 2 mm x 1.5 mm pieces and attached to a 96-well cell culture plate. human retinal pigmented epithelium cells (Human ARPE19 cells) seeded with 3,000 on the reference, negative control (PI film), positive control (puromycin-treated cells), and artificial retina and cultured at 37 °C, 5% CO <sub>2</sub> for 7 days. The positive control was treated with puromycin at a concentration of 0.5 µg/ml. To harvest cultured cells on artificial retinal devices and PI films, the devices and films were detached with forceps, transferred to 1.5 ml tubes, and treated with 0.25% trypsin/EDTA. The reference and puromycin-treated positive controls were harvested by treating the cells on the plates with 0.25% T/E. Harvested cells were double stained using the Annexin V conjugated with fluorescein isothiocyanate (FITC) and propidium iodide in the kit (Annexin V-FITC Apoptosis Detection kit, Sigma-Aldrich) for 10 minutes in the dark at room temperature. |
| Instrument                | Flow cytometry analysis was performed by using BD FACS Verse II (Becton Dickinson and company)   |
| Software                  | Data were acquired in BD FACSuite software and analysed in FlowJo software.  |
| Cell population abundance | For analysis, 10,000 cells were recorded from each sample.   |
| Gating strategy           | Cells were first gated to exclude debris (using FSC-A vs SSC-A), then gated for singlet (using FSC-H vs FSC-W and SSC-H vs SSC-W, sequentially). Gating was set up to use reference and positive control (puromycin-treated cells) (PI negative vs PI positive and FITC negative vs FITC positive, respectively).  |

- Tick this box to confirm that a figure exemplifying the gating strategy is provided in the Supplementary Information.